3D printing of open-porous cellular ceramics with high specific strength

Johannes Maurath[*], Norbert Willenbacher

Karlsruhe Institute of Technology, Institute for Mechanical Process Engineering Mechanics ,76131, Karlsruhe, Germany

A B S T R A C T

We present a novel processing route for manufacturing highly open porous, hierarchically structured ceramics via direct ink writing. We manufactured cellular samples with overall porosities up to 88% that exhibit fully open-porous struts with porosities between 45 and 60% and pore sizes $x_{50,3} < 6\,\mu m$ using capillary suspension based inks. An innovative processing strategy enabled manufacturing crack-free, undeformed cellular ceramic samples.

We printed hexagonal honeycomb structures that showed exceptionally high specific strength under compression load and significantly enlarged the strength-density range that was covered by sintered capillary suspensions, so far. Without loss of mechanical strength the density of ceramic parts was decreased by about a factor of 2–3. Strength of in-plane and out-of-plane loaded hexagonal honeycomb structures varies according to common scaling laws for cellular structures. The honeycombs are mechanically more efficient than bulk specimens from capillary suspensions, since they show a distinctly lower sensitivity of strength on density.

© 2017 Elsevier Ltd. All rights reserved.

1. Introduction

Highly porous ceramic materials with low density are extensively used in various technical applications, including filtration membranes for processes with hot or chemical reactive media, catalyst supports, energy storage systems, tissue-engineering scaffolds or lightweight construction materials [1–4]. The structure of a porous material strongly determines its properties and this also defines the field of application. Generally, we can distinguish between open and closed porous structures, while open porous ceramics exhibit a high permeability with a high accessible surface area, and closed-porous structures show good thermal insulation properties [5,6]. Engineering materials with a tailored mechanical strength at low densities are often inspired by natural materials, like wood, weed or cancellous bone, that are hierarchically structured [7–9]. These materials consist of lattice-like architectures that define cells in the mm-range, while the struts may be porous as well with pores in the μm-range, or they are complex composite materials [7,10–12]. 3D printing is a common way for manufacturing ceramic structures with well-defined cell geometry in the mm-range, but controlling also the porosity in the struts is a great

challenge up to now. This is especially valid for fully open-porous structures that are not only a high-strength structural ceramic, but also a functional material.

3D printing methods enable the fast and versatile manufacturing of prototypes, products at low number of units and tailor-made products. Next to ceramic parts [13,14], also polymers [15] and metals [13] and even food-products [16], are manufactured with 3D printing processes. However, 3D printing of ceramics is challenging due to complex process requirements. Typically, fabrication of dense ceramic components is addressed, but also porous ceramic materials are fabricated, especially for medical products like tailor-made implants or bone scaffolds [13,14,17,18], since these products cannot be manufactured economically via common processes like injection molding. A common 3D printing technique for porous ceramics is the so-called direct ink writing (DIW) where the desired body is assembled by specifically depositing small amounts of an ink or a paste [19]. This can be realized by a filamentary-based approach, like robocasting [13,20] and fused deposition modeling [14,20], or by a droplet-based approach, such as ink-jet printing [21,22].

Various processes are established for processing porous ceramic materials, including direct foaming, sacrificial templating, partial sintering, and using sacrificial fugitives [5,6]. Most of these techniques were originally developed for manufacturing macroporous bulk ceramics, but are partially combined with 3D printing

techniques to achieve custom shaped, hierarchically structured ceramics. Porous calcium phosphate granules have been used in combination with a sugar solution as organic binder to fabricate scaffold structures suitable for bone tissue engineering with porous struts (microporosity 60%) via 3D printing. Quadratic grid structures with mesh sizes in the order of 150–750 μm were obtained. The overall porosity was about 75% and the mechanical compressive strength was below 1 MPa not suitable for carrying high loads [23]. Garcia et al. [24] have synthesized very complex scaffold materials with a hierarchical pore structure ranging from 4 nm to 400 μm. They combined a sol-gel process including a surfactant providing the nm-sized pores, biopolymer sacrificial templating (methylcellulose) to achieve 30-80 μm pores, and direct ink writing of a suitable paste finally creating large 400 μm pores. In this case an overall porosity of about 40% was achieved. A printed structure including a regular arrangement of large pores with aligned microporous struts was obtained via 3D co-extrusion of a frozen alumina/camphene feed stock. The overall porosity of these scaffolds was 67–77% and the compressive strength varied between 10 and 30 MPa [25].

Direct ink writing processes also enable to create lightweight construction materials with distinct mechanical properties. Lewis et al. [11] reported about cellular structures made from fiber-filled epoxy resins with mechanical properties approaching the unique specific mechanical strength of balsa wood. This was accomplished due to the orientation of added silicon carbide and carbon fibers achieved during DIW and a distinct printed cellular structure. Another bio-inspired approach to obtain highly porous and high strength materials was presented by Fu et al. [26] Glass scaffolds with 60–80% porosity and a strength of 40–130 MPa under out-of-plane compression could be fabricated via DIW using a hydrogel based glass ink. However, in these latter approaches the printed struts did not include pores. Fabricating similar cellular structures with highly porous struts are an intriguing option to clearly enlarge the available specification range and to achieve lightweight materials with higher overall porosities and high specific strength. Recently, Muth et al. [12] as well as Minas et al. [10] published a concept for 3D printing hierarchically structured, lightweight ceramic solids with inks based on ceramic foams. Both authors used foams stabilized by surface modified Al_2O_3 particles. Muth et al. [12] presented cellular lightweight parts with closed-porous struts that exhibit a high specific stiffness [>10^7 Pa/(kg/m^3)] tailored by the printed geometry. In contrast, Minas et al. [10] printed struts with closed *and* open porosity but did not try to improve the mechanical efficiency due to tailored cellular structure. Specimens with an open-porosity between 83 and 94% and a compressive strength between 3 and 16 MPa were achieved.

Successful implementation of DIW processes for rapidly patterning complex 3D architectures crucially depends on the design of appropriate inks. According to the literature well printable inks should show a yield stress $\tau_{y} > 100$ Pa and storage modulus G' > 10^4 Pa [10,27]. Higher values of τ_y and G' are even better to achieve a high shape accuracy of the printed structures [11]. Paste like *capillary suspensions* with their high τ_y (>200 Pa) [28,29], high G' (>10^5 Pa) [30] and strong shear thinning behavior [29] are a promising platform for designing DIW inks [10,11]. Recently Dittmann et al. [29,31] developed a versatile new processing route based on capillary suspensions as precursors for manufacturing highly porous and mechanically stable ceramics. Capillary suspensions are ternary fluid/fluid/solid systems with a strong particle network structure controlled by capillary forces. When a small amount of a second, immiscible fluid is added to the continuous phase of a suspension, texture and flow of the admixture are dramatically altered due to the formation of a strong particle network within the suspension. Particles stick together due to capillary forces induced by liquid bridges formed by the secondary fluid. This phenomenon not

only alters the rheology of the system, it also stabilizes the suspension. Settling is prevented since particles are trapped in the network [32]. Such capillary suspensions were successfully used as a precursor for manufacturing porous sintered materials [28,29,31,33]. The bulk fluid can be removed from the suspension without collapse of the particle network that forms the backbone of the subsequently sintered part, since the remaining liquid bridges between particles formed by the secondary fluid largely provide the integrity of the structure if the pair of fluids is chosen appropriately. Following thermal debinding and sintering steps transfer the highly open-porous precursor into sintered a part with a high porosity and a uniform pore structure. This new processing route gives access to a broad range of pore structures including previously hardly accessible porosity and pore size ranges (porosity $\varepsilon > 50\%$, median pore diameter by volume $x_{50,3} < 10$ μm) with a very high repeatability regarding pore structure.

In this article we report about development of ceramic capillary suspension based inks for filament based DIW. We discuss sample preparation and composition providing stability, homogeneity and rheological properties enabling a stable DIW process. Then a method to transfer the printed specimen into sintered parts. Especially the latter step is the most crucial one since crack-formation and deformation during drying has to be prohibited for mechanical stable and functional sintered parts. We manufactured cellular structures in the shape of log-piles as well as hexagonal honeycombs. The first were primary for evaluating printing behavior while the latter were for mechanical testing. The nature inspired hierarchical, honeycomb structure promises excellent mechanical strength at low density.

2. Experimental procedure

2.1. Raw materials

Commercial grade aluminum oxide (α-Al_2O_3) particles were obtained from Almatis GmbH (CT3000SG) and Sumitomo Chemical (AKP-50). The average particle size according to the manufacturer is $x_{50,3} = 0.5$ μm for CT3000SG and $x_{50,3} = 0.2$ μm for AKP-50. Both particle types have a density of $\rho = \sim 3.9$ g/cm^3 and exhibit an arbitrary, isometric shape.

As bulk phase we used a mixture of highly liquid paraffin ($\eta = 0.035$ Pa s, $\rho = 0.85$ g/cm^3; Merck KGaA), odorless mineral spirits ($\rho = 0.752$ g/cm^3; Sigma-Aldrich) and palm wax ($\rho = 1.0$ g/cm^3; Candle Wiz; received from A.C. Moore, Somervile, USA). The composition of the bulk phase was: 48.6 vol% paraffin, 50.3 vol% mineral spirits and 1.1 vol% palm wax. The wax was dissolved in the two liquid phases by mixing the components in a planetary mixer (Speedmixer DAC 600.2; FlackTek Inc.) for 10 min at 2350 rpm. The melting temperature of the palm wax is $T_m = 80$–$87 °C$. The bulk phase mixture has a surface tension of $\Gamma_s = 25.4 \pm 0.2$ mN/m.

The secondary phase was a mixture of 50 vol% D(+)-sucrose (Carl Roth) in pure water. The aqueous sucrose solution has a surface tension of $\Gamma_s = 77.3 \pm 0.1$ mN/m.

We determined the three-phase contact angle θ_{SB} of the secondary fluid towards the α-Al_2O_3 particle surface using the Young-Duprée equation [34] with the surface tensions of the surrounding bulk phase $\Gamma_{Ba} = 25.4 \pm 0.2$ mN/m and the secondary phase $\Gamma_{Sa} = 77.3 \pm 0.1$ mN/m, the interfacial tension of the two fluids $\Gamma_{SB} = 28.3 \pm 0.3$ mN/m, and the contact angles of the fluids on Al_2O_3 against air $\theta_{Sa} = 55 \pm 3°$ and $\theta_{Ba} = 0°$. The calculations result in a three-phase contact angle of $\theta_{SB} = 47 \pm 9°$. Thus, the secondary phase preferentially wets the alumina particles and the capillary suspensions within this work are in the pendular state [32].
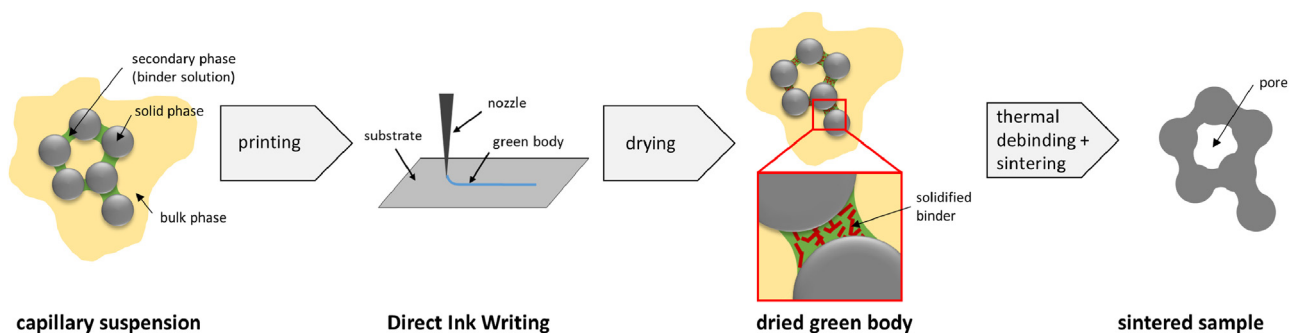
Fig. 1. Flow sheet of the processing route for direct ink writing of capillary suspension based inks. The open-porous structure of the sintered filaments is based on the open-porous network of capillary suspensions that serve as precursor for the ceramic part.

Table 1
Printing parameters for different ink compositions and nozzle diameters.

composition	nozzle diameter	translation velocity	volumetric flow rate
CT3000SG, $\phi_{sec}/\phi_{solid} = 0.165$	200 μm	42 mm/s	0.5 ml/min
CT3000SG, $\phi_{sec}/\phi_{solid} = 0.165$	250 μm	40 mm/s	0.5 ml/min
CT3000SG, $\phi_{sec}/\phi_{solid} = 0.165$	610 μm	55 mm/s	1.2 ml/min
AKP-50, $\phi_{sec}/\phi_{solid} = 0.1$	610 μm	55 mm/s	1.2 ml/min

2.2. Sample preparation, printing, and sintering procedures

Suspensions were prepared by mixing alumina particles into the bulk phase in a planetary mixer. We mixed a sample volume of 50 ml in 100 ml cups for 1 min at 800 rpm and 2 min at 2000 rpm. Subsequently, the secondary fluid was added and the suspension was mixed for 2 min at 2000 rpm. The emerging capillary suspension was homogenized for 14–20 h in a ball mill (long roll jar mill; US Stoneware) to prevent agglomerates. We used spherical grinding media with 25 mm ball diameter (zirconia balls; Inframat Advanced Materials). Solids content of suspensions with CT3000SG and AKP-50 particles was $\phi_{solid} = 31$ vol% and $\phi_{solid} = 23$ vol%, respectively. The ratio of secondary liquid to solid volume was $\phi_{sec}/\phi_{solid} = 0.165$ for capillary suspensions based on CT3000SG particles and $\phi_{sec}/\phi_{solid} = 0.1$ for suspensions based on AKP-50 particles.

Fig. 1 shows the processing steps for manufacturing ceramic structures via filamentary based direct ink writing. The capillary suspensions were extruded through tapered nozzles (inner diameters of: 200 μm, 250 μm, 610 μm; Nordson EFD). A syringe pump (PHD Ultra; Harvard Apparatus) was mounted on a custom made 3D positioning station (ABG 10000; Aerotech Inc.) for extruding the inks at a constant volumetric flow rate. 10 ml syringes (with Luer-Lok tip; BD) were loaded with the capillary suspension based ink and installed on the syringe pump. For loading syringes with bubble-free ink we opened the back of the syringe and loaded it with ink using a spatula. After each portion of added material fitful movements of the syringe (e.g. hitting the syringe slightly towards the edge of a table) forwarded the ink to the syringe tip without entrapped air bubbles. This is possible due to the high degree of shear thinning of capillary suspension type pastes. For translation in x-y-z direction the positioning station was programmed, while the syringe pump enabled printing at constant volumetric flow rate. Printing parameters, i.e. translation velocity and volumetric flow rate, are summarized in Table 1.

The capillary suspension based inks were printed on rectangular glass slides (75 × 50 mm), coated with a thin layer of polyethylene glycol (PEG 1500, Sigma-Aldrich). For a homogeneous PEG layer the glass slides as well as the polyethylene glycol were heated up to T = 90 °C, and afterwards the PEG was spread with a razorblade to a smooth and homogeneous layer. We printed so-called log-pile structures as well as cellular honeycomb structures on the coated glass slides. The log-pile structures had dimensions of 25 × 25 mm in green state and consisted of 10–16 printed layers. These structures are excellent test structures to evaluate the printing behavior of an ink, since they consist of many spanning elements that break due to deliquescence or bend strongly if the rheological properties of the ink are not appropriate. The log-pile structures were printed with nozzle diameters of 200, 250 and 610 μm. Cellular honeycombs were printed with 200 and 610 μm nozzles and had dimensions between 23 × 34 × 8 mm and 60 × 40 × 8 mm in green state. The honeycomb structures consisted of 10–20 printed layers. To control the overall porosity of the structures we varied the number and size of the hexagonal cells. The honeycomb structures typically exhibited between 8 and 50 hexagonal cells. Fig. 2 exemplarily shows a green body on a glass slide coated with PEG.

After printing of the ceramic specimen was finished the PEG layer was wetted with pure water around the sample as well as in the pores. Fig. 2 shows this step schematically. Afterwards, the green body was dried in a laboratory oven at T = ~94 °C for 15 min. This allows for evaporation of the mineral spirit in the bulk phase of the specimen and leads to a strong decrease of the palm wax solubility in the bulk phase. Even a small temperature drop below the melting point (80–87 °C) of the wax immediately induces crystal-
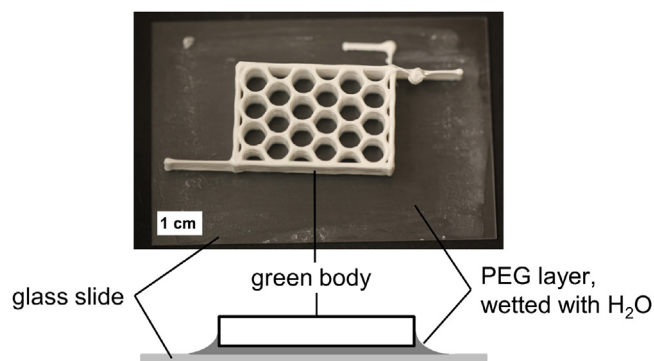

Fig. 2. Top view image of a green body. The specimen is printed on a glass slide coated with polyethylene glycol (PEG 1500). The PEG layer was wetted with pure water before the drying step was performed in a laboratory oven at T = ~94 °C for 15 min. The schematic side view shows the printed body, the lubrication layer and the support during drying.

lization. The slippery PEG/water layer enables the sample to shrink in the xy-plane and prohibits adhesion on the substrate during drying. After drying the green body was exposed to room temperature for 30–60 s allowing for crystallization of the palm wax in the residual bulk phase. The specimen were stable enough to move them gently onto a porous ceramic sintering plate, while the slippery PEG/water layer was still liquid and served as lubricating film.

Organic binder components in the green bodies were burned out in a debinding furnace. The samples were heated from room temperature to 200 °C at a rate of 2 °C/min. Subsequently, the temperature was held constant for 1 h at 200 °C. Afterwards, the temperature was increased to 700 °C with 1 °C/min and was held for 1 h at 700 °C. Finally, the oven was cooled down to 400 °C with 1.5 °C/min. After 15 min at a constant temperature of 400 °C, the oven was further cooled down to room temperature without temperature regulation.

For sintering we used a custom made high temperature furnace. Sintering temperatures were between 1200 and 1400 °C. The furnace was heated up to the sintering temperature at 3 °C/min. The final temperature was held constant for 2 h. Subsequently, the furnace cooled down to 50 °C at 2 °C/min.

2.3. Measurements

Rheological measurements were performed with a stress-controlled rheometer (Haake Mars II, Thermo Fisher Scientific, Karlsruhe, Germany). Plate-plate geometry (upper plate: titanium, lower plate: stainless steel) with a diameter of 35 mm was used. Both plates were rough (sandblasted surface) to prevent wall slip. The experiments were conducted at a gap height of 1 mm at T = 20 °C.

Porosity of the struts ε_s of the sintered cellular specimen was determined using the Archimedes' principle according to DIN EN 993-1. True porosity of the cellular ceramics ε^* was calculated from sample dimensions and sample weight.

Dimensions of printed struts and pores in green bodies and sintered parts were determined via manual image analysis using a light microscope.

Scanning-electron-microscope (SEM) micrographs (S-4500; Hitachi High-Technologies Europe GmbH) of the surface and of the crosscut of sintered parts were used to analyze their microstructure. Pore size was calculated via image analysis using the Line Intercept Count Method [35]. Therefore, SEM micrographs of sample cross sections were examined. To prepare appropriate cross sections of sintered parts we infiltrated them with epoxy resin, cured the resin at elevated temperature (70 °C for 20 h), and grinded and polished the specimens afterwards.

For compressive strength tests the honeycomb structures were grinded to a fully flat surface. Preliminary tests confirmed that vertical boundaries do not affect mechanical strength, so we did not remove these parts from all specimens. Compressive strength tests of cellular honeycombs were performed with material testing machines (Zwick Roell). The samples were loaded displacement controlled at a rate of 0.05 mm/s for the 10 kN load cell (machine model: ProLine Z010) and 0.05 mm/min for the 300 kN load cell (machine model: Zwick 300) until they failed.

3. Results and discussion

3.1. Rheology

We observed gel-like, pasteous behavior and a high yield stress in capillary suspensions based on CT3000SG and AKP-50 particles. Texture and gel-strength of the suspensions change strongly with addition of the secondary liquid. Fig. 3 shows the texture of a
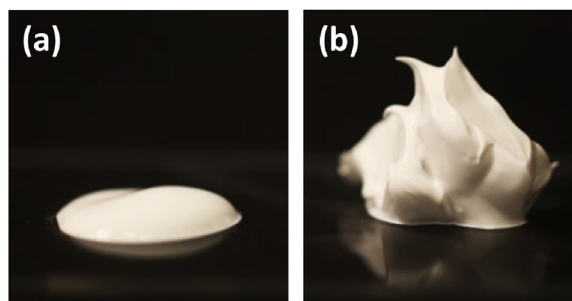
Fig. 3. Image of (a) a freely flowing pure suspension (ϕ_{solid} = 31 vol%, ϕ_{sec}/ϕ_{solid} = 0) and (b) a capillary suspension (CT3000SG, ϕ_{solid} = 31 vol%, ϕ_{sec}/ϕ_{solid} = 0.165) based on CT3000SG particles. Paste (b) shows excellent printing behavior.

pure suspension and an appropriate capillary suspension. The latter keeps the shape without any deliquescence and it consequently shows excellent printing behavior.

Rheological measurements proofed the gel-like behavior of both suspensions. We performed oscillatory shear experiments for pure suspensions as well as capillary suspensions based on the alumina powders CT3000SG and AKP-50. Paste composition was adjusted such that suspensions from both material systems show similar rheological and hence similar printing behavior. Due to the smaller size of AKP-50 particles a lower particle volume fraction was sufficient compared to the CT3000SG system to get suspensions as well as capillary suspensions with similar properties [36]. A solids content of ϕ_{solid} = 31 vol% for CT3000SG and ϕ_{solid} = 23 vol% for AKP-50 based suspensions was chosen. Furthermore, the ratio of secondary liquid to solid volume was set to ϕ_{sec}/ϕ_{solid} = 0.165 and ϕ_{sec}/ϕ_{solid} = 0.1 for capillary suspensions based on CT3000SG and AKP-50 particles, respectively.

Fig. 3a exemplarily shows the storage and loss moduli, G' and G", for the CT3000SG based suspension with and without added secondary fluid. In both cases the moduli are independent of frequency in the whole investigated range (ω = 0.1–100 rad/s) and G' is about one order of magnitude larger than G". Adding the secondary fluid, however, results in a transition from a weak to a strong gel with an almost three orders of magnitude increase in modulus (from 10^3 Pa to 10^6 Pa). Similar results were fund for the AKP-50 based system (G' increased from 10^3 Pa to 10^6 Pa).

The yield stress τ_y is an important indicator for evaluating the printing behavior of a paste since pastes with high yield stress are less prone to deliquescence of printed filaments [10,11]. We determined the yield stress τ_y of the suspensions via oscillatory shear amplitude sweep measurements at a constant frequency of ω = 1 rad/s. Fig. 4 exemplarily shows the data for the CT3000SG particle based system. At a certain stress amplitude G' and G" drop drastically from the plateau in the linear viscoelastic regime (LVE). This drop indicates the transition of the suspension from solid to fluid-like behavior [30]. We define a drop of G' for more than one decade compared to the plateau in the LVE regime as the criterion to determine the onset of yielding and the corresponding stress amplitude value is treated as the apparent yield stress τ_y. For CT3000SG particles the yield stress of the pure suspension is τ_y = 8.8 ± 2.5 Pa and of the capillary suspension τ_y = 2287 ± 157 Pa. For AKP-50 suspensions the yield stresses are τ_y = 5.1 ± 1.6 Pa and τ_y = 2131 ± 148 Pa, respectively. The yield stress of the capillary suspension is for both material systems more than two orders of magnitude larger than that of the corresponding pure suspension.

These results are in agreement with prior works on capillary suspensions [36,37]. The high yield stress and storage modulus values for the capillary suspensions result from the strong percolating particle network consisting of capillary bridges that is much stronger than the van der Waals network that is predominant in
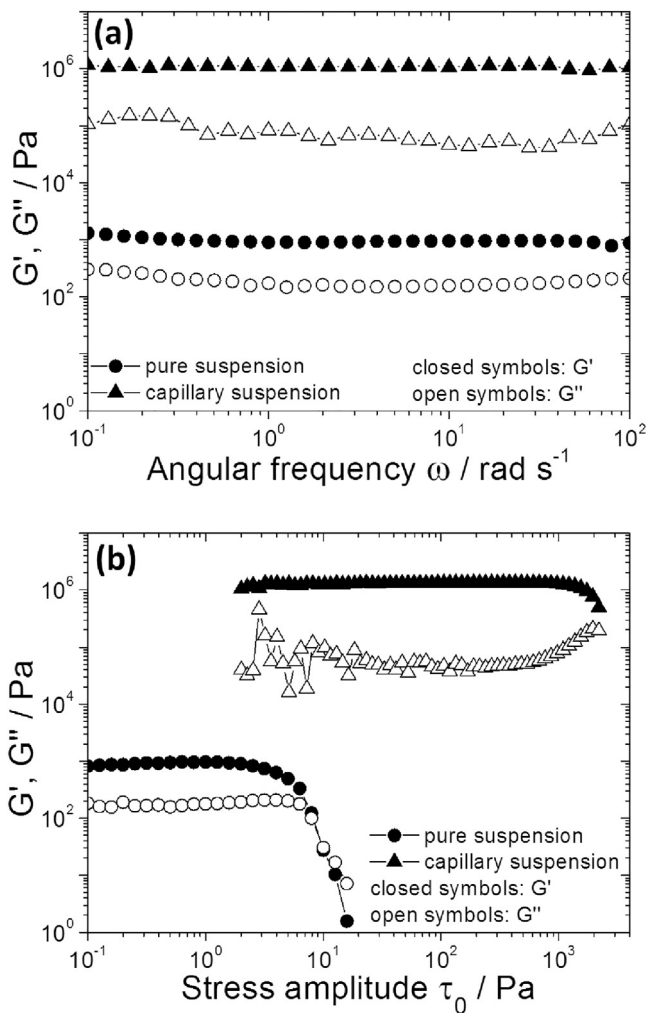
Fig. 4. Rheological data from oscillatory shear experiments of a pure suspension (CT3000SG, $\phi_{solid} = 31$ vol%, $\phi_{sec}/\phi_{solid} = 0$) and a capillary suspension (CT3000SG, $\phi_{solid} = 31$ vol%, $\phi_{sec}/\phi_{solid} = 0.165$). (a) Storage modulus G' and loss modulus G" are plotted vs. angular frequency ω. Stress amplitude τ_0 was 0.5 Pa for the pure suspension and 10 Pa for the capillary suspension. (b) Storage modulus G' and loss modulus G" plotted vs. shear stress amplitude τ_0 at fixed angular frequency ω = 1 rad/s.

Fig. 5. Schematic of the printed log-pile structures. Blue shaded areas mark the printed pores. (For interpretation of the references to colour in this figure legend, the reader is referred to the web version of this article.)

the pure suspensions. In steady shear experiments we observed a strong wall-slip for the capillary suspension based inks. Furthermore, capillary suspensions are known to exhibit strong shear thinning [28,31,38] and an immediate structural recovery after shearing [37]. These rheological features are ideal prerequisites for 3D printable pastes that can be extruded easily through small nozzles, and at the same time lead to stable extruded filaments without uncontrolled deliquescence, due to the high τ_y and G' [10–12,27].

3.2. Hierarchical ceramics

We printed cellular log-pile structures as well as honeycomb structures with capillary suspension based inks including AKP-50 and CT3000SG particles. Log-pile structures were printed for judging the printing behavior of the pastes. These structures exhibit tiny spanning elements and thus they are common in ink development for testing on deliquescence and stability of printed filaments from DIW processes. Fig. 5 shows a schematic of these printed structures that consist of multiple layers of printed filaments where the filaments of each layer are perpendicular to that of the layer below. Capillary suspension based inks showed good behavior for extruding thin filaments through small nozzles (200–610 μm) without
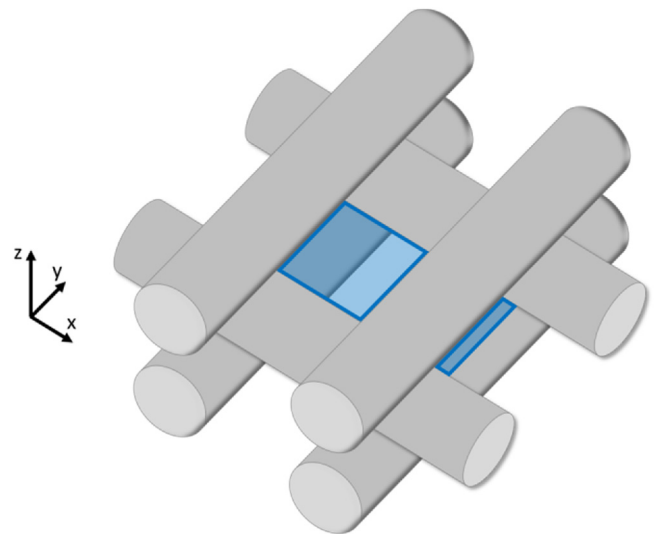
unwanted deliquescence, while printing of pure suspensions was not feasible at all. Extruded filaments did not hold shape and deliquesced instantly. With capillary suspension based inks it was possible to create spanning elements that bridge up to 2 mm.

Accuracy in shape for pores in the xy-plane was excellent for capillary suspensions printed with all tested nozzle diameters. Printed pores in the xy-plane had dimensions between 490 and 570 μm. For pores in the xz- and yz-plane the print quality differed depending on the selected nozzle diameter. Prints from 200 and 250 μm nozzles partially exhibited closed pores, while all prints from the 610 μm nozzle were excellent. The worse print quality with decreasing nozzle diameter may result from material overflow at the nozzle during extrusion. This results from too high volumetric flow rates of the inks or too low translation velocities of the nozzle. We monitored this material overflow by measuring the strut width of green bodies with a light microscope and related this to the nozzle diameter. Dried green bodies (drying conditions: 94 °C, 15 min, cf. Fig. 2) from CT3000SG suspensions that were printed with the 250 μm nozzle had strut widths of 490.5 ± 33.1 μm, while samples from 610 μm nozzles had strut widths of 634.5 ± 44.4 μm. The ratio of dried strut width to nozzle diameter is for small nozzles nearly twice as high as for the larger nozzles. However, further iteration of printing parameters is necessary to reach good printing results for feature sizes ≤ 250 μm.

Furthermore, we printed hexagonal honeycomb structures for lightweight construction materials mimicking natural materials with high specific mechanical strength, like wood [7]. These structures were used for mechanical tests, later on. Capillary suspension based inks were printed with 200 μm and 610 μm nozzles. The honeycombs exhibit large aspect ratio structures with wall height to width ratios in range of 4–11. Typically, wall thicknesses were 0.7-1.5 mm and heights 6–8 mm. The large aspect ratio structures did not show any deformation resulting from deliquescence.

All cellular green bodies were dried, thermally debinded and sintered. The samples shrank uniformly (10–26%) during the debinding and sintering process and did not show any macroscopically visible defects or deformations, as shown in Fig. 6. The small filaments poking out of the log-pile structures (top right of Fig. 6a) show the end point of 3D printing, where the nozzle departs from the specimen with high velocity. The filaments poking out of the cellular honeycombs (top right and bottom left of Fig. 6c) result from the chosen 3D printing procedure that includes additional
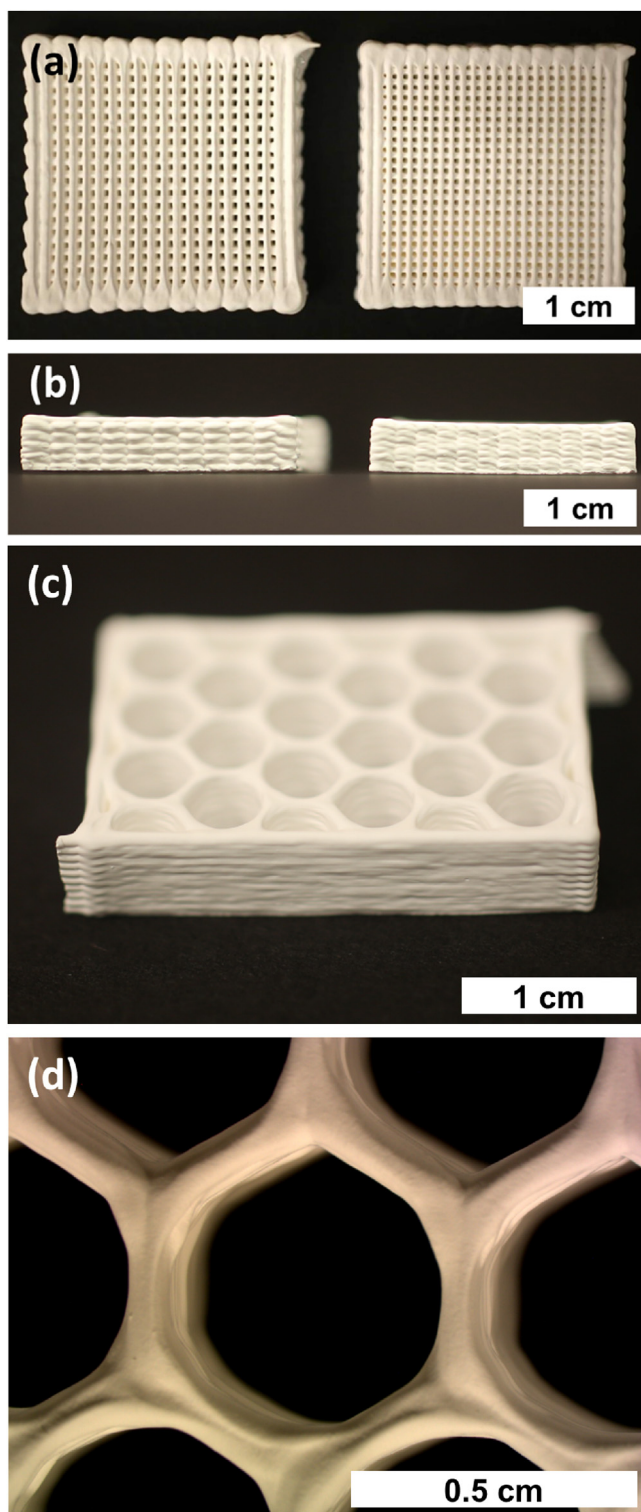
Fig. 6. Images of sintered cellular specimens from capillary suspensions based on CT3000SG powder. (a) Top view of a log-pile structure printed with a 610 μm nozzle (left) and a 250 μm nozzle (right). Printing parameters are summarized in Table 1. Geometrical settings for the structure shown on the left: distance between adjacent filaments = 1830 μm (=3x nozzle diameter), layer height = ~730 μm (= 1.2 x nozzle diameter); geometrical settings for the structure on the right: distance between adjacent filaments = 1000 μm (=4x nozzle diameter), layer height = 300 μm (=1.2x nozzle diameter). (b) Side view on the two log-pile structures. The sintered bodies show no deformation and are free of cracks. The left sample consists of 10 printed layers, the right one of 16. (c) And (d) are hexagonal honeycomb structures, printed with a nozzle diameter of 200 μm. Sintering conditions: T_s = 1300 °C, 2 h.

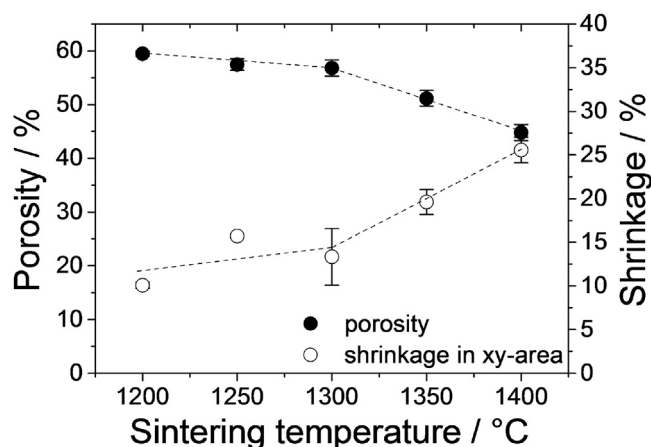Fig. 7. Strut porosity ε_s and shrinkage in xy-plane vs. sintering temperature (t = const. = 2 h) of specimens printed with different nozzle diameter (200–610 μm). The data shown are average values of at least 3–5 honeycombs or log-pile structures. The samples are made from CT3000SG particles. Strut porosity measurements were performed according to DIN EN 993-1.

print paths and dwell times for each printed layer, this procedure prevents nozzle clogging and guarantees high printing quality.

Flawless cellular honeycomb specimens were manufactured up to green body dimensions of approximately $60 \times 40 \times 8$ mm with true porosity in a range of $\varepsilon^* = 60\text{-}88\%$. True porosity ε^* of the cellular structure was varied by changing cell size, cell number, sample dimensions and sintering conditions, which directly impact the strut porosity ε_s.

Strut porosity ε_s as well as shrinkage of the cellular samples were controlled by the sintering temperature. Both parameters occurred to be independent of printed geometry or nozzle diameter, indicating that the microstructure of the ceramic is not affected by the printing process. Porosity measurements confirmed that the struts are fully open-porous in agreement with previous work on capillary suspension based porous sintering materials [28,29,31,33]. Fig. 7 shows how strut porosity decreases with increasing sintering temperature, while shrinkage of the samples increases in xy-plane. The strut porosities were in a range of $\varepsilon_s = 59.5 \pm 0.5\%$ and $45.7 \pm 1.8\%$ for sintering temperatures between 1200 and 1400 °C. Shrinkage in the xy-plane was between 10 and 26%. Up to a sintering temperature of 1300 °C porosity and shrinkage barely vary. For T >1300 °C, however, sintering is strongly accelerated and porosity strongly decreases while shrinkage increases substantially.

As mentioned earlier the sintered cellular parts are flawless and do not show any defects, even microscopically. Top view SEM images of the samples, Fig. 8a and b, show a smooth and crack-free surface of the printed filaments that are well connected to perpendicular filaments on the layer below. Even at the junctures no cracks are visible. The higher magnification in Fig. 8b reveals the open-porous surface of the filaments and a homogeneous, narrow pore size distribution. SEM images of crosscut sections, Fig. 8c and d, are better to visualize the microstructure of the porous struts. Fig. 8c shows a crosscut of a log-pile sample that was printed with a nozzle diameter of 610 μm. The cross-cut filaments are nearly circular in shape and the printed pores in xy- and yz-plane (cf. blue shaded areas in Fig. 5) are fully open. Fig. 8d shows a crosscut of a porous strut at a higher magnification. The pore structure of the sintered struts is similar to that of typical capillary suspension based moulded glass [28] or ceramic membranes [29,31,33]. We determined the pore size distribution of sintered struts via SEM image analysis of cross sections. Table 2 summarizes the $x_{50,3}$ as well as $x_{10,3}$ and $x_{90,3}$
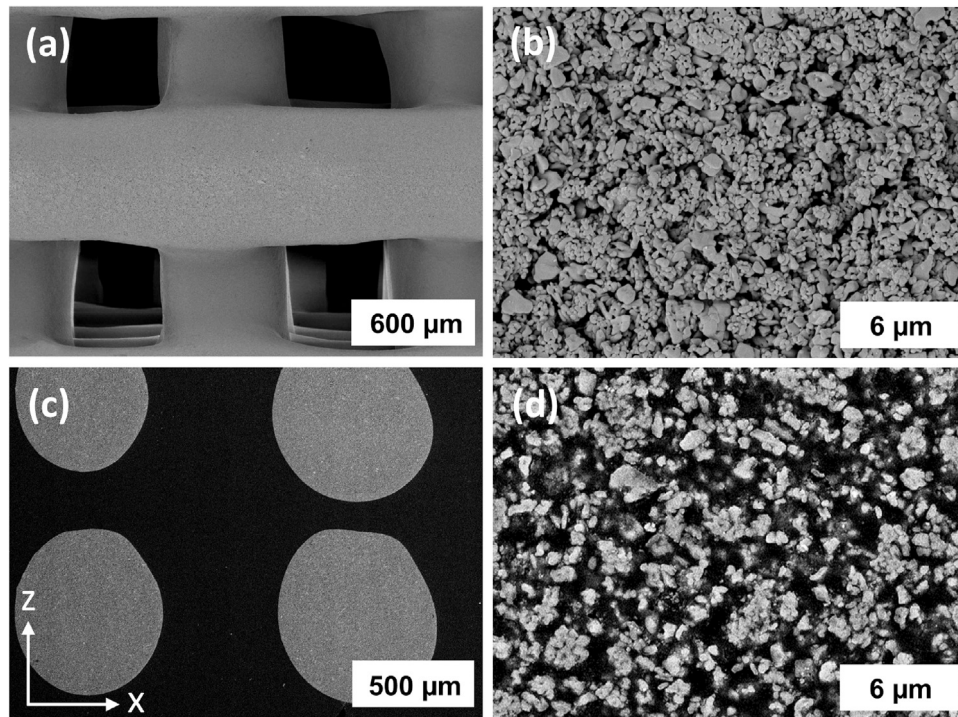
Fig. 8. SEM images of sintered log-pile structures based on capillary suspensions from CT3000SG particles, printed with a 610 μm nozzle. (a) Top view and (b) magnified surface of printed filaments. (c) Crosscut image of printed filaments. The coordinate system is equivalent to that in Fig. 5. (d) Crosscut image with the unique microstructure of sintered capillary suspensions. Sintering conditions: T_s = 1300 °C, 2 h.

Table 2
Microstructural properties of sintered parts based on capillary suspensions.

material	sintering conditions	strut porosity ε_s	pore size $x_{10,3}$	pore size $x_{50,3}$	pore size $x_{90,3}$
Almatis, CT3000SG	1200 °C, 2 h	59.5 ± 0.5%	2.4 ± 0.0 μm	5.3 ± 0.7 μm	8.3 ± 0.1 μm
Almatis, CT3000SG	1300 °C, 2 h	56.3 ± 1.6%	2.4 ± 0.0 μm	5.7 ± 0.4 μm	10.0 ± 0.0 μm
Almatis, CT3000SG	1400 °C, 2 h	45.7 ± 1.8%	1.8 ± 0.0 μm	4.8 ± 1.0 μm	9.5 ± 0.1 μm
Sumitomo, AKP 50	1300 °C, 2 h	55.4 ± 1.6%	0.7 ± 0.1 μm	1.9 ± 0.6 μm	3.2 ± 0.2 μm

values for samples based on CT3000SG and AKP-50 particles sintered at different sintering temperatures T_S. The average pore size $x_{50,3}$ as well as the pore size distribution width $(x_{90,3}-x_{10,3})$ of CT3000SG samples changes from $x_{50,3}$ = 5.3 ± 0.7 μm at T_s = 1200 °C to $x_{50,3}$ = 4.8 ± 1.0 μm at T_s = 1400 °C, consistent with decrease in porosity from 59.5 ± 0.5% to 45.7 ± 1.8% shown in Fig. 7. At constant sintering conditions (T_S = 1300 °C, 2 h) the ink based on the smaller AKP-50 particles yields a smaller average pore size of $x_{50,3}$ = 1.9 ± 0.6 μm (compared to $x_{50,3}$ = 4.8 ± 1.0 μm for the CT3000SG system) as expected [29], while the relative width of pore size distribution, $(x_{90,3}-x_{10,3})/x_{50,3}$ = 1.32 and 1.58, respectively, and porosity are almost the same.

3.3. Mechanical properties

Compressive strength of a honeycomb structure is strongly influenced by the overall density ρ^* of the sample. Fig. 9 shows typical engineering stress-strain curves of selected samples with different ρ^*. The samples were loaded perpendicular to the cell orientation ("in-plane"). Structures consisted of 18 hexagonal cells and were printed with a 200 μm nozzle. Dimensions of all three samples were similar in the green state; the overall density ρ^* was varied by changing the sintering temperature. The initial non-linear increase in stress for strains <0.015 may result from orientation of the experimental setup at low loads [39]. The stress-strain graph allows for calculating the Young's modulus E from the slope of the respective curve, but in this work we focus on the compres-

sive strength σ^*, i.e. the maximum load that the sample can resist without fracturing.

The honeycomb structures printed here show superior mechanical strength at low relative density ρ^*/ρ_m (with m for matrix, i.e.
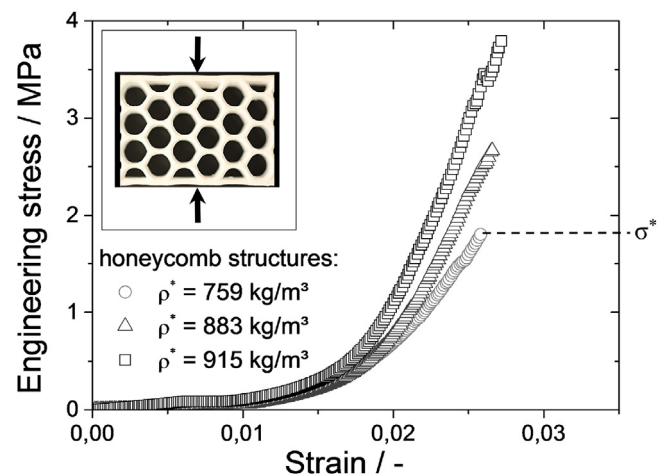

Fig. 9. Engineering stress vs. strain curves of honeycomb structures loaded perpendicular to cell orientation in compression test. The dashed line exemplarily indicates the compressive strength σ^* (i.e. stress at failure) for one sample. The insert schematically shows a honeycomb in compression test.
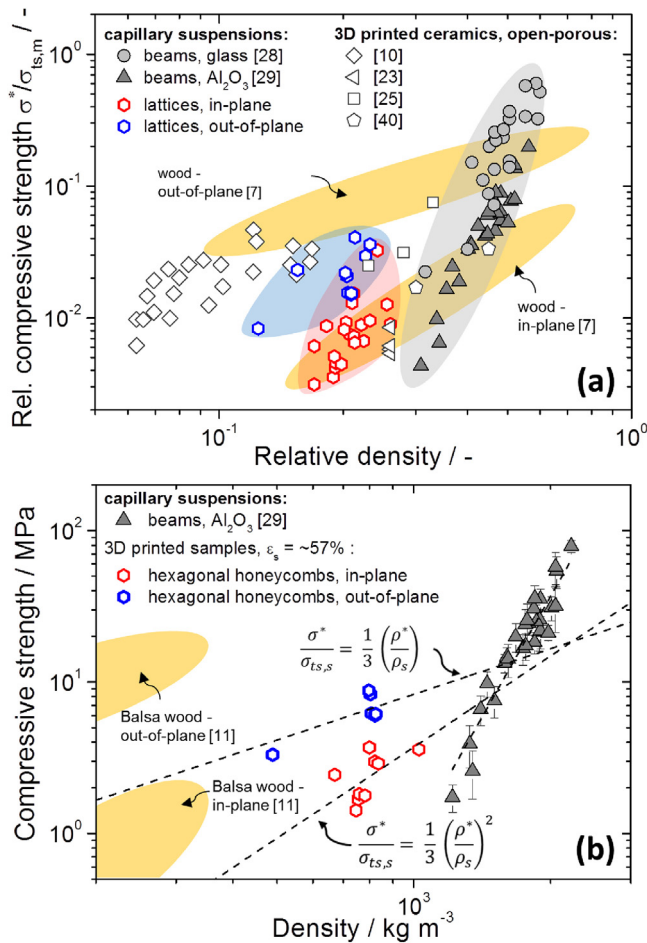
Fig. 10. Mechanical strength data of the 3D printed honeycomb structures. One data point represents the result of one tested sample in compression strength test. (a) Relative compressive strength vs. relative density for honeycomb structures and other 3D printed ceramics and glasses that exhibit fully open-porous struts [10,23,25,28,29,40]. The orange shaded areas show the characteristic rel. strength – rel. density range of wood [7]. (b) Compressive strength as a function of density. The graph shows data for honeycomb structures with constant strut porosity $\varepsilon_s = \sim 57\%$ and slip-cast specimens based on capillary suspensions from Dittmann et al. [29]. The dependence of strength on density for the 3D printed samples fits well to the scaling laws for in-plane and out-of-plane loaded hexagonal honeycomb structures [43]. The orange shaded areas show the characteristic strength – density range of Balsa wood [11]. (For interpretation of the references to colour in this figure legend, the reader is referred to the web version of this article.)

here Al_2O_3 with $\rho_m = 3.9 \, g/cm^3$) compared to slip-cast beams of sintered capillary suspensions made from Al_2O_3 [29] and glass [28] as well as to other open-porous ceramics manufactured via 3D printing processes [23–25,40]. Fig. 10a shows the compressive strength σ^* of the specimens normalized to the tensile strength of the matrix material $\sigma_{ts,m}$, thus excluding material specific differences in strength vs. relative density ρ^*/ρ_m. For the honeycomb structures, σ^* is only a function of ρ^*, and not of sample geometry (number and size of cells, sample dimensions) varied to change overall density. The honeycombs show equal relative strength $\sigma^*/\sigma_{ts,m}$ at lower relative density ρ^*/ρ_m compared to most ceramics from 3D printing processes that show open-porous struts [23–25,40]. Only the recently published results for 3D printed, open-porous alumina foams from Minas et al. [10] showed a higher specific mechanical strength. This might be due to a more round and thus smoother pore shape of these latter parts. Our ceramic honeycomb structures based on capillary suspensions even reach the relative strength to relative density range that is covered by wood [7], which is a highly appreciated lightweight construc-

tion material, at least under in-plane load. However, wood gains its high mechanical strength from the strong cell walls and the strength gain due to the cellular structure is lower than for ceramic structures. As shown in Fig. 10b, considering absolute values the specific strength of the ceramic honeycombs fabricated from capillary suspensions approach that of Balsa wood, the prime example of wood with high specific strength [7,11]. However, other cellular structures manufactured in 3D printing processes exhibit distinctly higher specific strength than the open porous ceramics presented here, but in all cases their struts are either dense or of closed porosity [10,26,39,41,42]. Instead, 3D printed open porous structures offer additional opportunities with respect to filtration or catalysis applications.

With the cellular structures obtained from 3D printing we decreased the overall density ρ^* of sintered capillary suspensions by about a factor of 2–3 compared to uniform bars or disks without losing mechanical strength. Relative densities ρ^*/ρ_m of the cast beams and 3D printed honeycomb structures are in the range of 0.3–0.56 ($\rho^* = 1200–2200 \, kg/m^3$) and 0.12-0.25 ($\rho^* = 490–1000 \, kg/m^3$), respectively. Overall porosities ε^* are between 43 and 70% and 75–88%. Exemplarily picking a honeycomb structure loaded perpendicular to cell orientation ("in-plane") with a density of $\sim 790 \, kg/m^3$, this specimen shows the same compressive strength of $\sim 3 \, MPa$ as a slip-cast specimen with a clearly higher density of $\sim 1330 \, kg/m^3$. This effect gets even stronger when we load the honeycomb structures parallel to cell orientation ("out-of-plane"). The structures behave highly anisotropic and a similar strength ($\sim 3 \, MPa$) is achieved now at a density of only $\sim 490 \, kg/m^3$. In turn, at a given density strength increases by a factor 2–3 comparing in-plane to out-of-plane loading.

As can be seen from Fig. 10b, the compressive strength of hexagonal honeycombs is well described by [7–9]

$$\frac{\sigma^*}{\sigma_{ts,s}} = C \left(\frac{\rho^*}{\rho_s} \right)^k \tag{1}$$

where σ^* is the compressive strength of the honeycomb, $\sigma_{ts,s}$ is the tensile strength of the struts, ρ^* is the true density of the honeycomb, ρ_s is the strut density, and C and k are constants that depend on type of cellular structure and loading direction. For hexagonal honeycombs $C = 1/3$ while $k = 2$ and 1 for in-plane [7,9] and out-of-plane [7,8] loading, respectively. This scaling model is based on the mechanisms of failure of hexagonal cellular structures under load. For in-plane loading these structures are nearly ideal bending-dominated lattices ($k = 2$), while for out-of-plane loading they show ideal stretch-dominated behavior ($k = 1$) [43]. Generally, stretch-dominated structures exhibit a higher stiffness and strength than bending-dominated structures. This anisotropic behavior is well-known for biological hierarchical cellular structures such as wood, weed or bones [7,8].

Fig. 10b shows a set of data for hexagonal honeycombs with various overall densities ρ^*, but constant strut porosity of $\varepsilon_s = 57\%$, in a compressive strength versus density representation. The scaling law introduced in Eq. (1) with exponents $k = 2$ for in-plane loaded specimens and $k = 1$ for out-of-plane loaded specimens describes the dependence of strength on density very well. We focus on the scaling here, determination of the pre-factor C is not possible here, since this would require knowledge of the tensile strength of the porous struts $\sigma_{ts,s}$ not available so far. For porous ceramics this quantity is in general hardly accessible, since brittle materials tend to undefined stresses in the tensile test thus causing erroneous results. However, the term $\sigma_{ts,s} C \left(\frac{1}{\rho_s} \right)^k = C^*$ is constant if strut density ρ_s as well as tensile strength $\sigma_{ts,s}$ of the porous struts are constant [29], as it is the case here. From a fit of Eq. (1) to the data in Fig. 10b we determine C^* and with $\rho_s = 1694 \, kg/m^3$ (i.e. $\varepsilon_s = \sim 57\%$) as well as $C = 1/3$ we estimate consistent tensile strength values

$\sigma_{ts,s} = 31 \pm 3$ MPa and $\sigma_{ts,s} = 42 \pm 3$ MPa from the in-plane and out-of-plane data sets, respectively. This seems to overestimate the true tensile strength of the struts expected to be about a factor of 5–10 lower than the compressive strength [44] which in our case is $\sim$20 $\pm$ 5 MPa [29].

However, the scaling laws describe the density dependence of mechanical strength of the hexagonal honeycomb structures very well. In both cases of loading, in-plane and out-of-plane, the 3D printed structures are mechanically more efficient than cast beams, strength of slip-cast samples is significantly more sensitive to a decrease of density than the lattice structures. This high mechanical efficiency of lattice structures was also reported by Minas et al. [10] and Muth et al. [12] who successfully used different ink compositions, emulsions and foams including ceramic particles, instead of capillary suspensions for direct ink writing of hierarchically structured cellular solids as well as by Compton et al. [11], who manufactured triangular honeycombs from organic composite materials.

4. Conclusions

We introduced a processing route for manufacturing hierarchically structured, highly open-porous cellular structures with high specific strength. We developed inks based on ceramic capillary suspensions that show excellent printing behavior for 3D printing cellular structures with high aspect ratios (height/width = 4–11) as well as small spanning elements. The ink concept is versatile and can be applied to a wide range of ceramic particles with different particle size, while rheological behavior of the ink can be adjusted easily according to printing and processing demands in a wide range. We successfully used a filamentary based direct ink writing technique for printing cellular ceramic structures with nozzle diameters $\geq$200 μm. An innovative processing strategy enabled us to debind and sinter these filigree structures without crack formation or undesired deformation of the specimens. Hierarchically structured, cellular samples with overall porosities in the range of 60–88% were produced. The printed struts are fully open porous ($\varepsilon_s = 45$–60%) and show average pore sizes $x_{50,3} < 6$ μm.

We printed ceramic hexagonal honeycomb structures that show exceptionally high specific strength compared to common capillary suspension based ceramics and to most 3D printed open porous ceramics from other processes. The overall density of the honeycomb structures is significantly decreased compared to slip-cast uniform samples, but the cellular structure still guaranteed a high mechanical strength in compression. Specific strength of the honeycomb structures is about a factor of 2–3 larger than the strength of cast specimens. Honeycomb structures behave anisotropic under compression load, and the compressive strength of in-plane loaded samples is about 2–3 times larger than that of out-of-plane loaded specimens. The obtained compression strength data are very well described by commonly accepted scaling laws.

The concept introduced here offers further opportunities for fabrication of cellular solids with even higher mechanical strength in the range of e.g. Balsa wood, one of the prime examples for natural cellular materials with unique specific strength [11]. Two promising strategies are to use the so-called smart capillary suspension concept [33] to reinforce the sintering necks in the porous struts finally resulting in a higher overall mechanical strength or to use capillary suspensions based on glass particles yielding smoother pore structure beneficial for high mechanical strength at low density [28].

Beyond that the open porous hierarchical structures spanning the length scales from 10^{-3} m to 10^{-7} m enabled by DIW of capillary suspension type ceramic inks may find application in separation and filtration processes, e.g. as microfluidic crossflow filters for hot gas filtration or as catalyst supports with smart flow channels for fast chemical reactions requiring high internal surface.

References

[1] P. Colombo, Conventional and novel processing methods for cellular ceramics, Philos. Trans. R. Soc. A 364 (2006) 109–124.

[2] F. Akhtar, L. Andersson, S. Ogunwumi, N. Hedin, L. Bergström, Structuring adsorbents and catalysts by processing of porous powders, J. Eur. Ceram. Soc. 34 (2014) 1643–1666.

[3] E.C. Hammel, O.-R. Ighodaro, O.I. Okoli, Processing and properties of advanced porous ceramics: an application based review, Ceram. Int. 40 (2014) 15351–15370.

[4] W.-Y. Yeong, W.Y. Yeong, C.-K. Chua, C.K. Chua, K.-F. Leong, K.F. Leong, et al., Rapid prototyping in tissue engineering: challenges and potential, Trends Biotechnol. 22 (2004) 643–652.

[5] T. Ohji, M. Fukushima, Macro-porous ceramics: processing and properties, Int. Mater. Rev. 57 (2012) 115–131.

[6] A.R. Studart, U. Gonzenbach, E. Tervoort, L. Gauckler, Processing routes to macroporous ceramics: a review, J. Am. Ceram. Soc. 89 (2006) 1771–1789.

[7] L.J. Gibson, The hierarchical structure and mechanics of plant materials, J. R. Soc. Interface 9 (2012) 2749–2766.

[8] L. Gibson, M. Ashby, Cellular Solids: Structure and Properties, Cambridge University Press, Cambridge, UK, 1997.

[9] N.A. Fleck, V.S. Deshpande, M.F. Ashby, Micro-architectured materials: past, present and future, Proc. R. Soc. A Math. Phys. Eng. Sci. 466 (2010) 2495–2516.

[10] C. Minas, D. Carnelli, E. Tervoort, A.R. Studart, 3D printing of emulsions and foams into hierarchical porous ceramics, Adv. Mater. (2016).

[11] B.G. Compton, J.A. Lewis, 3D-printing of lightweight cellular composites, Adv. Mater. 26 (2014) 5930–5935.

[12] J.T. Muth, P.G. Dixon, L. Woish, L.J. Gibson, J.A. Lewis, Architected cellular ceramics with tailored stiffness via direct foam writing, Proc. Natl. Acad. Sci. (2017) (201616769).

[13] A. Zocca, P. Colombo, C.M. Gomes, J. Günster, Additive manufacturing of ceramics: issues, potentialities, and opportunities, J. Am. Ceram. Soc. 98 (2015) 1983–2001.

[14] N. Guo, M.C. Leu, Additive manufacturing: technology, applications and research needs, Front. Mech. Eng. 8 (2013) 215–243.

[15] B. Wendel, D. Rietzel, F. Kühnlein, R. Feulner, G. Hülder, E. Schmachtenberg, Additive processing of polymers, Macromol. Mater. Eng. 293 (2008) 799–809.

[16] J.I. Lipton, M. Cutler, F. Nigl, D. Cohen, H. Lipson, Additive manufacturing for the food industry – a review, Trends Food Sci. Technol. 43 (2015) 114–123.

[17] VDI, Statusreport – Additive Fertigungsverfahren, 2014.

[18] K.F. Leong, C.M. Cheah, C.K. Chua, Solid freeform fabrication of three-dimensional scaffolds for engineering replacement tissues and organs, Biomaterials 24 (2003) 2363–2378.

[19] J.A. Lewis, Direct ink writing of 3D functional materials, Adv. Funct. Mater. 16 (2006) 2193–2204.

[20] J. Deckers, J. Vleugels, J.-P. Kruth, Additive manufacturing of ceramics: a review, J. Ceram. Sci. Technol. 5 (2014) 245–260.

[21] E.M. Sachs, M.J. Cima, P.A. Williams, D. Brancazio, J. Cornie, Three dimensional printing: rapid tooling and prototypes directly from a CAD model, J. Manuf. Sci. Eng. 114 (1992) 481–488.

[22] J. Song, M. Edirisinghe, J. Evans, Formulation and multilayer jet printing of ceramic inks, J. Am. Ceram. Soc. 82 (1999) 3374–3380.

[23] H. Seitz, U. Deisinger, B. Leukers, R. Detsch, G. Ziegler, Different calcium phosphate granules for 3-D printing of bone tissue engineering scaffolds, Adv. Eng. Mater. 11 (2009) 41–46.

[24] A. Garcia, I. Izquierdo-Barba, M. Colilla, C.L. De Laorden, M. Vallet-Regi, Preparation of 3-D scaffolds in the SiO2-P2O5 system with tailored hierarchical meso-macroporosity, Acta Biomater. 7 (2011) 1265–1273.

[25] Y.W. Moon, I.J. Choi, Y.H. Koh, H.E. Kim, Porous alumina ceramic scaffolds with biomimetic macro/micro-porous structure using three-dimensional (3-D) ceramic/camphene-based extrusion, Ceram. Int. 41 (2015) 12371–12377.

[26] Q. Fu, E. Saiz, A.P. Tomsia, Bioinspired strong and highly porous glass scaffolds, Adv. Funct. Mater. 21 (2011) 1058–1063.

[27] J.E. Smay, J. Cesarano III, J.A. Lewis, Colloidal inks for directed assembly of 3-D periodic structures, Langmuir 18 (2002) 5429–5437.

[28] J. Maurath, J. Dittmann, N. Schultz, N. Willenbacher, Fabrication of highly porous glass filters using capillary suspension processing, Sep. Purif. Technol. 149 (2015) 470–478.

[29] J. Dittmann, N. Willenbacher, Micro structural investigations and mechanical properties of macro porous ceramic materials from capillary suspensions, J. Am. Ceram. Soc. 97 (2014) 3787–3792.

[30] J. Maurath, B. Bitsch, Y. Schwegler, N. Willenbacher, Influence of particle shape on the rheological behavior of three-phase non-Brownian suspensions, colloids surfaces a physicochem, Eng. Asp. 497 (2016) 316–326.

[31] J. Dittmann, E. Koos, N. Willenbacher, Ceramic capillary suspensions: novel processing route for macroporous ceramic materials, J. Am. Ceram. Soc. 96 (2013) 391–397.

[32] E. Koos, N. Willenbacher, Capillary forces in suspension rheology, Science 331 (2011) 897–900.

[33] J. Dittmann, J. Maurath, B. Bitsch, N. Willenbacher, Highly porous materials with unique mechanical properties from smart capillary suspensions, Adv. Mater. 28 (2016) 1689–1696.

[34] E. Koos, J. Johannsmeier, L. Schwebler, N. Willenbacher, Tuning suspension rheology using capillary forces, Soft Matter. 8 (2012) 6620.

[35] J. Russ, R. Dehoff, Practical Stereology, Kluwer Academic/Plenum Publishers, 2000.

[36] E. Koos, Capillary suspensions: particle networks formed through the capillary force, Curr. Opin. Colloid Interface Sci. 19 (2014) 575–584.

[37] E. Koos, W. Kannowade, N. Willenbacher, Restructuring and aging in a capillary suspension, Rheol. Acta 53 (2014) 947–957.

[38] B. Bitsch, J. Dittmann, M. Schmitt, P. Scharfer, W. Schabel, N. Willenbacher, A novel slurry concept for the fabrication of lithium-ion battery electrodes with beneficial properties, J. Power Sources 265 (2014) 81–90.

[39] J. Bauer, S. Hengsbach, I. Tesari, R. Schwaiger, O. Kraft, High-strength cellular ceramic composites with 3D microarchitecture, Proc. Natl. Acad. Sci. 111 (2014) 2453–2458.

[40] C. Polzin, D. Gunther, H. Seitz, 3D printing of porous Al2O3 and SiC ceramics, J. Ceram. Sci. Technol. 6 (2015) 141–145.

[41] X. Zheng, H. Lee, T.H. Weisgraber, M. Shusteff, J. DeOtte, E.B. Duoss, et al., Ultralight, ultrastiff mechanical metamaterials, Science 344 (2014) 1373–1377.

[42] L.R. Meza, S. Das, J.R. Greer, Lightweight and recoverable three – dimensional ceramic nanolattices, Science 345 (2014) 1322–1326.

[43] M.F. Ashby, The properties of foams and lattices, Philos. Trans. A. Math. Phys. Eng. Sci. 364 (2006) 15–30.

[44] Informationszentrum Technische Keramik, Brevier Technische Keramik, Fahner Verlag, Lauf, Germany, 2003.